

THE PENNSYLVANIA STATE UNIVERSITY
SCHREYER HONORS COLLEGE

DEPARTMENT OF PHYSICS

ANALYSIS OF A SAMPLE OF BL LAC OBJECTS WITH THE HAWC OBSERVATORY

ERICA LYNN HELLER
SPRING 2023

A thesis
submitted in partial fulfillment
of the requirements
for baccalaureate degrees
in Physics and Astronomy & Astrophysics
with honors in Physics

Reviewed and approved* by the following:

Miguel A. Mostafá
Professor of Physics and Astronomy & Astrophysics
Associate Dean of Research and Innovation
Thesis Supervisor

Richard W. Robinett
Professor of Physics
Associate Department Head and Director of Undergraduate Studies
Honors Adviser

*Signatures are on file in the Schreyer Honors College.

Abstract

Only three sources of extragalactic TeV gamma-ray emission have been observed by the High-Altitude Water Cherenkov (HAWC) Gamma-Ray Observatory. Using a pre-selected candidate list of potential TeV-emitting BL Lac objects, we searched for TeV emission using the 2321-day dataset from the HAWC Observatory. Eleven BL Lac objects were investigated. For four of these BL Lac objects, lower energy gamma-ray data was available from the Fermi Large Area Telescope (Fermi-LAT). Using data from Fermi-LAT, we fit a simple power law model to the energy spectrum of each source and used this simple power law model to investigate the region using HAWC. We found no significant TeV gamma-ray emission from these four sources. We set upper limits on the flux from these sources at 1 TeV. For the remaining seven sources, we used three simple power law models due to the lack of lower-energy gamma-ray data. We found no significant TeV gamma-ray emission from these seven sources using all three simple power law models, and we set upper limits on the flux from these sources at 1 TeV for each model. Despite the lack of gamma-ray detection from these sources, we determine that the upper limits set using HAWC data can constrain the extrapolation of a simple power law model into the TeV energy range for three of the four sources with Fermi-LAT data. Through these investigations of BL Lac objects, we provide valuable information about the acceleration mechanisms occurring at these extreme extragalactic objects.

Table of Contents

List of Figures	iv
List of Tables	v
Acknowledgements	vi
1 Introduction to Gamma-Ray Astronomy	1
1.1 Gamma-Ray Astronomy	2
1.1.1 Emission Mechanisms	2
1.1.2 Detection Methods	4
1.2 Observatories	6
1.2.1 Fermi Large Area Telescope	6
1.2.2 Cherenkov Telescope Array	7
1.2.3 High-Altitude Water Cherenkov Gamma-Ray Observatory	8
2 Introduction to Te-REX Sources	9
2.1 Active Galactic Nuclei	10
2.2 Te-REX: A Sample of Extragalactic TeV-emitting Candidates	10
2.2.1 Defining BL Lac Objects and Passive Elliptical Galaxies	11
2.2.2 HBLs with the Highest Chance of Detection by CTA	12
3 Methods	14
3.1 Searching for Extragalactic Very-High-Energy Gamma-Ray Sources with HAWC	15
3.2 Pre-Selected Candidate Sources	16
3.3 Significance and Flux Upper Limit Calculations	17
3.4 Methods for Candidate Sources with Fermi-LAT Data	18
3.5 Methods for Candidate Sources without Fermi-LAT Data	18
4 Results	19
4.1 Sources with Fermi-LAT Data	20
4.1.1 1REXJ123123+1421.3	20
4.1.2 1REXJ134105+3959.8	22
4.1.3 1REXJ141029+2820.9	24
4.1.4 1REXJ141756+2543.3	26
4.2 Sources without Fermi-LAT Data	29

4.2.1	1REXJ121510+0732.0	29
4.2.2	1REXJ142336+4826.1	30
4.2.3	1REXJ142645+2415.3	31
4.2.4	1REXJ145339+1804.2	32
4.2.5	1REXJ151924+2053.7	33
4.2.6	1REXJ160740+2541.2	34
4.2.7	1REXJ183200+5202.2	35
5	Conclusion	36
5.1	Conclusion	37
5.2	Future Work	37
	Bibliography	38

List of Figures

1.1	Synchrotron and Inverse Compton Emission Spectral Energy Distribution	3
1.2	Pion Decay Emission Spectral Energy Distribution	4
1.3	Gamma-Ray vs. Cosmic-Ray Showers	5
1.4	Gamma-Ray vs. Cosmic-Ray Showers with the HAWC Observatory	6
1.5	Artist's Conception of the Fermi Gamma-Ray Space Telescope	7
1.6	Prototype Telescope Designs for CTA	8
1.7	The HAWC Observatory	8
2.1	SED of BL Lac Object vs. SED of PEG	11
2.2	Modeled SED of 1REXJ123123+1421.3 with IACT Observatory Sensitivity Curves	12
3.1	All-sky Map from the HAWC Observatory	15
3.2	Sensitivity Curves of Various Telescopes and Observatories	16
4.1	Significance Map of 1REXJ123123+1421.3	21
4.2	Spectrum of 1REXJ123123+1421.3	22
4.3	Significance Map of 1REXJ134105+3959.8	23
4.4	Spectrum of 1REXJ134105+3959.8	24
4.5	Significance Map of 1REXJ141029+2820.9	25
4.6	Spectrum of 1REXJ141029+2820.9	26
4.7	Significance Map of 1REXJ141756+2543.3	27
4.8	Spectrum of 1REXJ141756+2543.3	28
4.9	Significance Maps of 1REXJ121510+0732.0	29
4.10	Significance Maps of 1REXJ142336+4826.1	30
4.11	Significance Maps of 1REXJ142645+2415.3	31
4.12	Significance Maps of 1REXJ145339+1804.2	32
4.13	Significance Maps of 1REXJ151924+2053.7	33
4.14	Significance Maps of 1REXJ160740+2541.2	34
4.15	Significance Maps of 1REXJ183200+5202.2	35

List of Tables

2.1	TeV-REX Sources Classified as “Good Candidates” for Detection by CTA	13
3.1	Pre-Selected Candidate Sources	17
4.1	Fermi-LAT Data for 1REXJ123123+1421.3	20
4.2	Parameter Values for Fit to the Fermi-LAT Data for 1REXJ123123+1421.3	20
4.3	HAWC Significance and Upper Limit for 1REXJ123123+1421.3	21
4.4	Fermi-LAT Data for 1REXJ134105+3959.8	22
4.5	Parameter Values for Fit to the Fermi-LAT Data for 1REXJ134105+3959.8	23
4.6	HAWC Significance and Upper Limit for 1REXJ134105+3959.8	23
4.7	Fermi-LAT Data for 1REXJ141029+2820.9	24
4.8	Parameter Values for Fit to the Fermi-LAT Data for 1REXJ141029+2820.9	25
4.9	HAWC Significance and Upper Limit for 1REXJ141029+2820.9	25
4.10	Fermi-LAT Data for 1REXJ141756+2543.3	26
4.11	Parameter Values for Fit to the Fermi-LAT Data for 1REXJ141756+2543.3	27
4.12	HAWC Significance and Upper Limit for 1REXJ141756+2543.3	27
4.13	HAWC Significance and Upper Limits for 1REXJ121510+0732.0	29
4.14	HAWC Significance and Upper Limits for 1REXJ142336+4826.1	30
4.15	HAWC Significance and Upper Limits for 1REXJ142645+2415.3	31
4.16	HAWC Significance and Upper Limits for 1REXJ145339+1804.2	32
4.17	HAWC Significance and Upper Limits for 1REXJ151924+2053.7	33
4.18	HAWC Significance and Upper Limits for 1REXJ160740+2541.2	34
4.19	HAWC Significance and Upper Limits for 1REXJ183200+5202.2	35

Acknowledgements

I was supported by the NASA Pennsylvania Space Grant Consortium's Women in Science and Engineering Research program from Spring 2020 through Spring 2021. I would like to thank Dr. Miguel Mostafá and Dr. Hugo Ayala for being incredible mentors throughout my time here and Dr. Richard Robinett for being an incredible adviser. I would also like to thank the HAWC collaboration for assisting me with access to data and their review of my conference presentations. Finally, I would like to thank my partner in the Women in Science and Engineering Research program, Maya Debski, for her work and support throughout this project.

Chapter 1

Introduction to Gamma-Ray Astronomy

1.1 Gamma-Ray Astronomy

Gamma rays are electromagnetic radiation with the highest energies on the electromagnetic spectrum. The emission of gamma rays has been linked to the most extreme objects and behaviors in the universe, including but not limited to supernovae, pulsars, and active galactic nuclei. These astrophysical phenomena have also been theorized to be the originators of charged particles accelerated to relativistic speeds, also known as cosmic rays. However, since cosmic rays are charged particles, their trajectories are altered by magnetic fields throughout the universe. Gamma rays are part of the electromagnetic spectrum and thus do not have charge, so their trajectories are not altered by magnetic fields on their way toward Earth from their original emission location. Their straight trajectories allow us to trace the origin of gamma rays, linking them to objects throughout the universe. The study of gamma rays reveals more information about these extreme conditions where cosmic rays are produced.

Gamma-ray radiation is produced through two major emission processes: leptonic emission and hadronic emission. Leptonic emission is produced through the interactions of accelerated electrons and positrons, and hadronic emission is produced through the interactions of accelerated protons. The energy distributions in the gamma-ray energy range observed by gamma-ray observatories reveal important information about the acceleration mechanisms occurring within these objects.

1.1.1 Emission Mechanisms

There are two main types of leptonic emission: synchrotron emission and inverse Compton emission. These emission methods present as two peaks on an electromagnetic spectrum spanning from radio to gamma-ray energies. Synchrotron emission is produced from the interaction of electrons and positrons with a strong magnetic field. The photons produced from synchrotron emission range in energy from radio to as high as low-energy gamma rays. Inverse Compton emission is produced through the interaction of electrons and positrons with low-energy photons. The interaction of these electrons and positrons with the low-energy photons can boost the energy of the photons up to very high energies, typically ranging from x-rays all the way to very-high-energy gamma rays [1].

The equation for synchrotron emission is given by Equation (1.1), where E_e is the energy of the electron, B is the magnetic field strength, and E_{sync} is the energy of the photon produced by the synchrotron emission [2]

$$E_{sync} = 0.2 \frac{B}{10\mu\text{G}} \left(\frac{E_e}{1\text{TeV}} \right)^2 \text{ eV}. \quad (1.1)$$

The energy distribution of electrons is typically given by a simple power law, $dN/dE = k(E_e/E_0)^{\alpha_e}$ with dN/dE representing flux, k equaling the flux at energy E_0 , and an index given by α_e . Thus, the synchrotron emission becomes represented by a simple power law with an index of $\alpha_{sync} = (\alpha_e + 1)/2$. Another important feature of a synchrotron peak is the break in the power law distribution. A break in the peak of the emission is caused by cooling of the electrons as synchrotron radiation is produced. The energy loss of electrons is proportional to E_e^{-1} , altering the index of the energy distribution of electrons from α_e to $\alpha_e + 1$. This break in the peak occurs at roughly $E_{e,br} = 1.2 \times 10^4 (B/10\mu\text{G})^{-2}$ [2].

The equation for inverse Compton emission is given by Equation (1.2) where E_e is the energy of the electron or positron, E_{ph} is the energy of the low energy photon, and E_{IC} is the energy of the boosted high energy photon [2]

$$E_{IC} = 5 \times 10^9 \frac{E_{ph}}{10^{-3} \text{ eV}} \left(\frac{E_e}{1 \text{ TeV}} \right)^2 \text{ eV.} \quad (1.2)$$

The distribution of the energy of electrons for inverse Compton is the same as for synchrotron: a simple power law distribution with index given by α_e . The inverse Compton emission can then be represented by a simple power law with index $\alpha_{IC} = (\alpha_e + 1)/2$. The peak present in the inverse Compton emission is caused by a process called Klein-Nishina (KN) cooling at high energies which causes an even steeper drop-off in the index of the energy distribution than for synchrotron. The KN cooling causes the simple power law index to become $\alpha_{IC} = \alpha_e + 1$. Figure 1.1 shows an example spectral energy distribution with synchrotron and inverse Compton emission peaks [2].

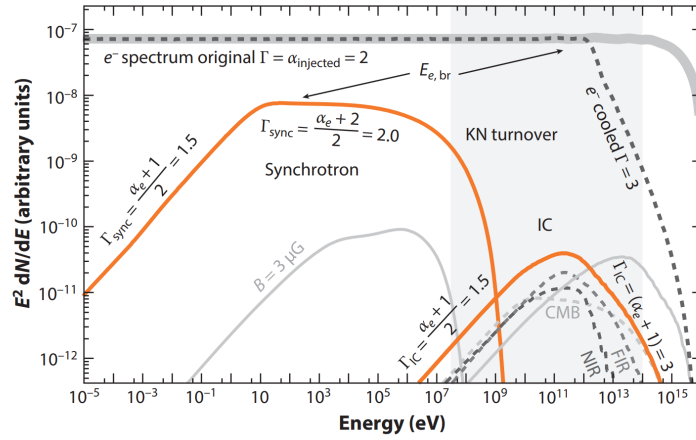


Figure 1.1: Synchrotron and Inverse Compton Emission Spectral Energy Distribution: energy distribution caused by synchrotron and inverse Compton emission (orange) for a sample electron energy distribution with index $\alpha_e = 2.0$ (light gray) [2].

The main form of hadronic emission of gamma rays is through the interaction of protons with matter, producing nuclear reactions. One of the products of these reactions is neutrally charged mesons (π^0) which then decay into gamma rays. Hadronic emission occurs most frequently in dense regions of the interstellar medium [1]. Equation (1.3) shows the equation of decay of a π^0 meson into two gamma rays:



The decay of the mesons into gamma rays turns the entire mass of the meson into energy, producing an amount of energy proportional to the mass, $E = mc^2$. The mass of the π^0 meson is $135 \text{ MeV}/c^2$, so the energy of each photon is $E_{ph} = 67.5 \text{ MeV}$ in the rest frame of the meson. The resulting spectrum produced by hadronic emission is thus a log-log function dependent on the energy spectrum of the original protons with a peak at 67.5 MeV , also known as the “pion-decay bump.” The “pion-decay bump” is unique to this form of hadronic emission and allows for some

characterization of the acceleration mechanism if present in the spectrum [2]. Figure 1.2 shows an example of a pion decay spectral energy distribution showing the characteristic “pion-decay bump.”

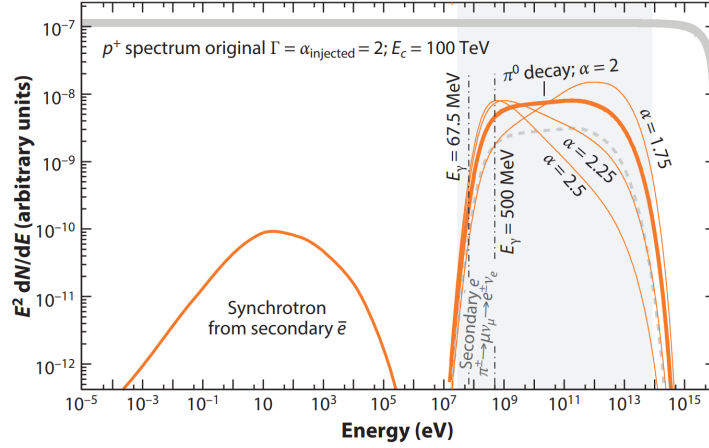


Figure 1.2: Pion Decay Emission Spectral Energy Distribution: energy distribution caused by pion decay emission (orange) for a sample proton energy distribution with index $\alpha_p = 2.0$ (light gray) [2].

1.1.2 Detection Methods

There are three types of detection methods in use for the collection of data on gamma-ray emission: direct detection, detection of Cherenkov light in the atmosphere, and detection of secondary particle showers on the ground. Direct detection of gamma rays is only possible from a space-based observatory, as gamma rays cannot pass through the Earth’s atmosphere without interacting with the atmosphere. However, space-based observatories have limited detection capabilities at very high energies. Different energy gamma rays require different detection areas of the telescopes. Higher energy gamma rays require a very large detection area due to their lower flux compared to lower energy gamma rays, so even the largest space-based gamma-ray observatories are limited to energies below ~ 300 GeV. Ground-based observatories are needed to observe very-high-energy gamma rays. These ground-based observatories do not directly detect gamma rays, but instead detect the secondary particles that are products of gamma-ray interactions with the Earth’s atmosphere [2]. Gamma rays interacting with the top of the Earth’s atmosphere create particle showers made up of electrons and positrons (Equation 1.4)

$$\gamma \rightarrow e^- + e^+. \quad (1.4)$$

Imaging atmospheric Cherenkov telescopes (IACT) detect optical Cherenkov light produced by these particle showers in the atmosphere, but IACTs are limited to detection only on clear, dark nights when the Cherenkov light is visible. Water Cherenkov detectors detect Cherenkov light produced inside water tanks when the secondary particles of the shower reach the ground. Water Cherenkov detectors have the advantage of having the ability to run at all times of day, but the energy of the gamma rays must be larger than ~ 100 GeV to be detected because the particles produced must be energetic enough to reach the ground. The combination of the three detection

methods allows for the entire gamma-ray spectrum to be observed across a significant portion of the sky [2].

Analysis of data spanning the entire gamma-ray spectrum provides valuable information about the acceleration mechanisms of the gamma-ray producing objects in the universe. However, to obtain the valuable information that gamma rays provide, these observatories must distinguish the emission caused by gamma rays from the very strong background emission caused by cosmic rays. Because of this strong cosmic-ray background, space-based gamma-ray observatories must actively discard events determined to be from charged particles, indicating a cosmic ray detection instead of a gamma ray detection. IACT and water Cherenkov observatories must use the differences in shower shapes and the presence of muons to determine the difference between cosmic-ray showers and gamma-ray showers [2]. The types of showers that IACT observatories would use to distinguish between cosmic-ray interactions and gamma-ray interactions with the top of the atmosphere are shown in Figure 1.3. This figure shows a simulated cosmic-ray shower and a simulated gamma-ray shower. The cosmic-ray shower is much larger than the gamma-ray shower and shows the presence of muons which have a larger horizontal velocity and thus travel farther away from the core of the shower.

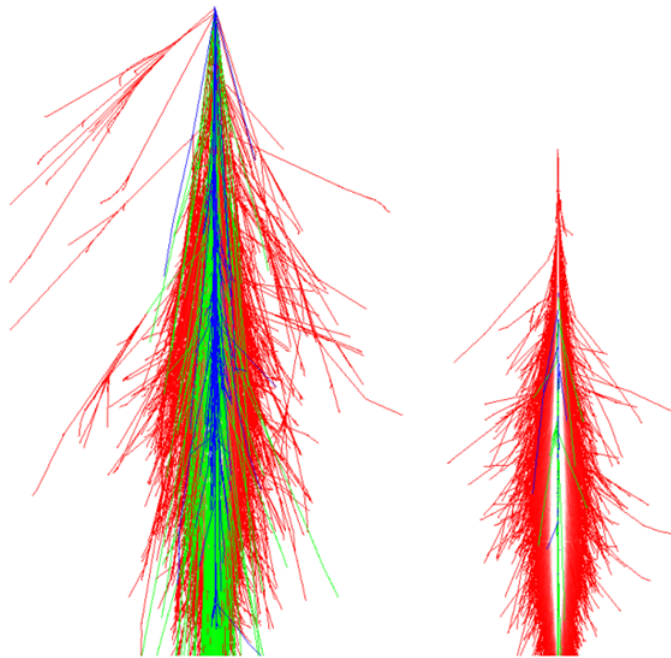


Figure 1.3: Simulation of a cosmic-ray shower (left) vs. simulation of a gamma-ray shower (right) [3].

Water Cherenkov observatories use the footprint of the shower on the array of water tanks to distinguish between cosmic-ray and gamma-ray showers. Figure 1.4 shows simulated cosmic-ray and gamma-ray showers for a water Cherenkov observatory. Cosmic-ray showers show the presence of muons far from the core of the shower while gamma-ray showers have most of the energy deposited close to the shower axis.

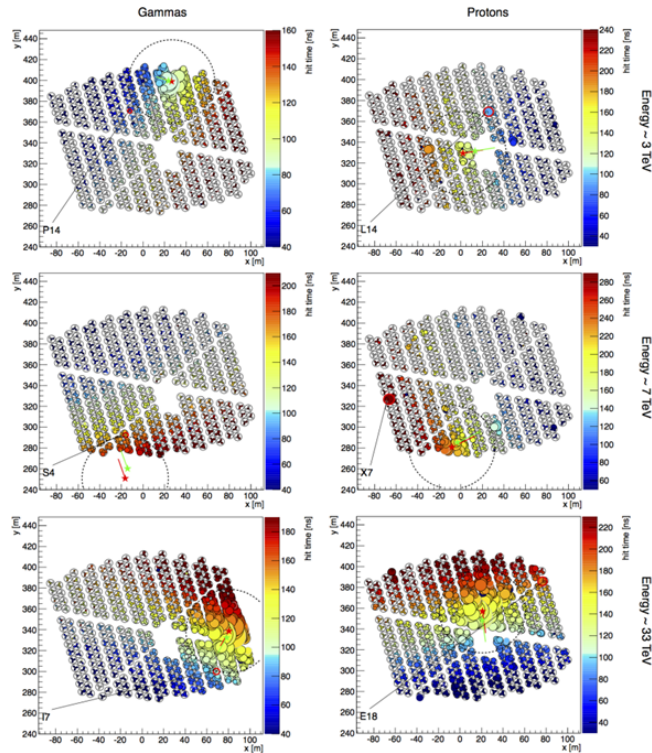


Figure 1.4: Simulation of cosmic-ray showers (right) vs. simulation of gamma-ray showers (left) for the water tank array of the High-Altitude Water Cherenkov Gamma-ray Observatory [4].

1.2 Observatories

Three main observatories will be referenced in this study: the Fermi Large Area Telescope, the Cherenkov Telescope Array, and the High-Altitude Water Cherenkov Gamma-Ray Observatory. The Fermi Large Area Telescope is a lower-energy gamma-ray observatory, providing low-energy gamma-ray data for the objects in this study. The Cherenkov Telescope Array has not yet been completed and no data has been collected by it, but previous astronomers used the expected sensitivity curve of this future telescope to predict the potential of the emissions from the objects in this study to be detected in the TeV energy range. This paper focuses primarily on data collected by the High-Altitude Water Cherenkov Gamma-Ray Observatory in the regions of the objects which will be introduced in Chapter 2.

1.2.1 Fermi Large Area Telescope

The Fermi Large Area Telescope (Fermi-LAT) is located on the Fermi Gamma-Ray Space Telescope in low-Earth orbit. In contrast to IACT and water Cherenkov observatories, space-based gamma-ray telescopes utilize the production of electrons and positrons from gamma rays in a controlled environment instead of observing the results of the production in the Earth's atmosphere. Fermi-LAT consists of 36 layers of silicon strips and 16 layers of tungsten foil. The tungsten foil facilitates the production of electron-positron pairs from gamma rays received by Fermi-LAT, and

the silicon strips act as detectors to track the electrons and positrons. Beneath the silicon strips are CsI crystals used to determine the energy of the detected gamma rays. Another detector consisting of photomultiplier tubes is used to reject data from background cosmic-ray interactions. Fermi-LAT has an energy range from 20 MeV to 300 GeV, a duty cycle of 76%, and a field of view of 2.4 sr [5]. Figure 1.5 shows an artist's conception of Fermi-LAT in orbit.



Figure 1.5: Artist's Conception of the Fermi Gamma-Ray Space Telescope [6].

Data from Fermi-LAT used in this study comes from the Third Source Catalog, or 3FGL catalog. The 3FGL catalog is a catalog of 3033 sources in the 100 MeV-300 GeV energy range. Nearly four years of data were collected for each source, from 2008-2012. This catalog, which is a public-use dataset, provides the fluxes and upper limits for four of the sources examined in this study [5].

1.2.2 Cherenkov Telescope Array

The Cherenkov Telescope Array (CTA) is a pair of future IACT arrays that, at the time of this study, is under construction. CTA will have an energy range of 20 GeV-300 TeV and consist of two sites: a northern array and a southern array. Three sizes of telescopes will be in use at the sites. The southern array will consist of small-sized, medium-sized, and large-sized telescopes while the northern array will consist of only medium-sized and large-sized telescopes. In total, 40 medium-sized telescopes, 8 large-sized telescopes, and 70 small-sized telescopes will be constructed across both sites. To detect Cherenkov light showers in the atmosphere, these telescopes will consist of mirrors that will reflect the light into the extremely sensitive cameras consisting of photomultiplier tubes. The large-sized telescopes will have an energy range of 20 GeV-150 GeV with a field of view of 4.3° , the medium-sized telescopes will have an energy range of 150 GeV-5 TeV with a field of view of $7.5-7.7^\circ$, and the small-sized telescopes will have an energy range of 5 TeV-300 TeV with a field of view of 10.5° [7]. Figure 1.6 shows four of the prototype designs for the CTA telescopes.

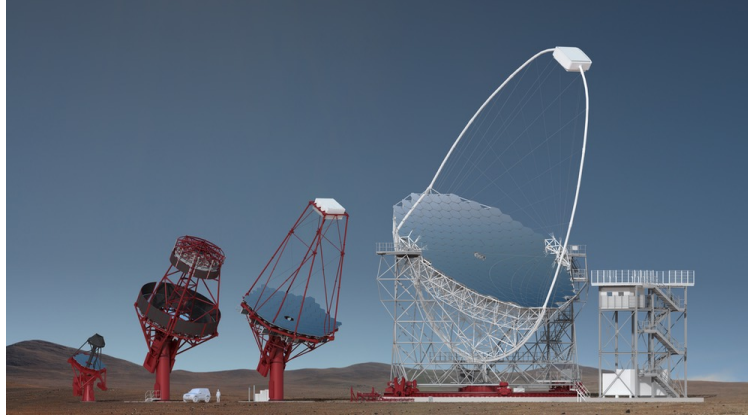


Figure 1.6: Prototype Telescope Designs for CTA; small-sized telescope on left, two versions of the medium-sized telescope in the center, and large-sized telescope on the right [7].

1.2.3 High-Altitude Water Cherenkov Gamma-Ray Observatory

The High-Altitude Water Cherenkov (HAWC) Gamma-Ray Observatory is a water Cherenkov observatory located at 19°N , 97°W and an altitude of 4100 meters in Puebla, Mexico [8]. HAWC consists of 300 water tanks, each holding 200,000L of purified water and four photomultiplier tubes. Particles created in the air showers create Cherenkov light inside the water tanks which is observed by the photomultiplier tubes. These showers can then be reconstructed and the energy and location of the gamma ray that caused the shower can be determined. HAWC has an energy range of 300 GeV to above 100 TeV, a duty cycle of 95%, and an instantaneous field of view of 2.0 sr [9]. The declination range of the field of view of HAWC is -26° to 64° . HAWC sees this declination range and the entire right ascension range every day, which is roughly two-thirds of the entire sky. This large field of view and nearly continuous duty cycle allows HAWC to observe many sources at the same time, gathering large datasets that can be analyzed without a need to point the observatory at any one point in the sky. This makes HAWC ideal for searching for new sources of TeV gamma-ray emission.



Figure 1.7: Side view [10] (left) and top view [11] (right) of the High-Altitude Water Cherenkov Gamma-Ray Observatory.

Chapter 2

Introduction to Te-REX Sources

2.1 Active Galactic Nuclei

An Active Galactic Nucleus (AGN) is defined as the region in the center of a galaxy that has a luminosity much higher than other galaxies, a majority of which comes from non-stellar origins. AGNs are divided into radio-quiet and radio-loud AGNs depending on their radio luminosity. Radio-loud AGNs are comprised of supermassive black holes with accretion disks and two ejection jets of relativistic particles perpendicular to the accretion disk, and radio-quiet AGNs have a similar structure but with no relativistic jets. Radio-loud AGNs are further split into two categories based on the angle between Earth and the relativistic jets. For angles greater than 20° , the radio-loud AGN is classified as a Radiogalaxy, and for angles smaller than 20° , the radio-loud AGN is classified as a Blazar. Blazars are then split into Flat Spectrum Radio Quasars (FSRQs) and BL Lacertae (BL Lac) objects depending on the strength of their emission lines in the optical spectrum, with FSRQs having the stronger emission lines [12].

Radio-loud AGNs have a distinct spectral energy distribution (SED), a plot of energy vs. frequency of light. The SEDs of radio-loud AGNs have a double-peaked SED ranging across almost the entire electromagnetic spectrum. The first peak is formed by synchrotron radiation in the relativistic jet, and the second peak is formed by inverse Compton emission. FSRQs and BL Lac objects show different features on their SEDs. FSRQs have higher luminosities with the two peaks located towards lower energies, while BL Lacs have lower luminosities with the two peaks located towards higher energies. BL Lac objects can further be separated into three categories based on the synchrotron peak. Low synchrotron-peaked BL Lac objects (LBLs) have the two peaks at lower energies than other BL Lac objects, but not as low as FSRQs. Intermediate synchrotron-peaked BL Lac objects (IBLs) feature peaks at slightly higher energies than LBL objects, and high synchrotron-peaked BL Lac objects (HBLs) have peaks at the highest energies of these objects. HBLs are the BL Lac objects with the most potential to be detected by very-high-energy (VHE) gamma-ray observatories due to this highest energy peak [12].

2.2 Te-REX: A Sample of Extragalactic TeV-emitting Candidates

“Te-REX: a sample of extragalactic TeV-emitting candidates” by Balmaverde *et al.* is a catalog of potentially VHE-emitting HBLs created by cross-matching x-ray and radio data of known blazars. The goal of this catalog was to compose an unbiased sample of HBLs as potential targets for the upcoming CTA. In this study, the authors did not rely on other catalogs of BL Lac objects, instead choosing to start from a catalog of Radio-Emitting x-ray sources (REX) and determining which objects had the characteristics of HBLs. Starting from 1600 REX sources, the authors narrowed down their sample by defining criteria for HBL objects to be studied further: they must be within the planned field of view of CTA, have a small value for the ratio of the radio-to-x-ray spectral index, have an optical magnitude of less than 21, and not be extended sources. This created a sample of 87 REX sources. These 87 sources were then analyzed in the optical range to determine a further classification. Objects with strong emission lines were discarded for the purposes of this paper as they would be most likely categorized as FSRQs, and objects with weak emission lines were divided into two categories: BL Lac objects and Passive Elliptical Galaxies (PEGs) [13].

2.2.1 Defining BL Lac Objects and Passive Elliptical Galaxies

The difference between BL Lac objects and PEGs was determined by the authors based on the Calcium II break, denoted by $K(\text{CaII})$, or the decrease in flux between the blue and red portion of the optical spectrum around 4000 Å. Equation (2.1) gives the equation for the calculation of $K(\text{CaII})$: [13]

$$K(\text{CaII}) = \left(1 - \frac{1}{D_n(4000)}\right) \times 100 \quad (2.1)$$

Where $D_n(4000)$ is the ratio of the average flux densities between 4050-4250 Å and 3750-3950 Å. For galaxies without an active nucleus, the $K(\text{CaII})$ value is around 50%, but for galaxies with an active nucleus, the value decreases due to the presence of non-thermal emission caused by the active nucleus. The authors define a BL Lac object as an object with a $K(\text{CaII})$ value less than 40% and a PEG as an object with a $K(\text{CaII})$ value greater than 40%. Figure 2.1 shows example SEDs for PEG and BL Lac objects. The lower non-thermal emission from the PEG causes the thermal emission from the host galaxy to dominate the spectra in the optical range [13].

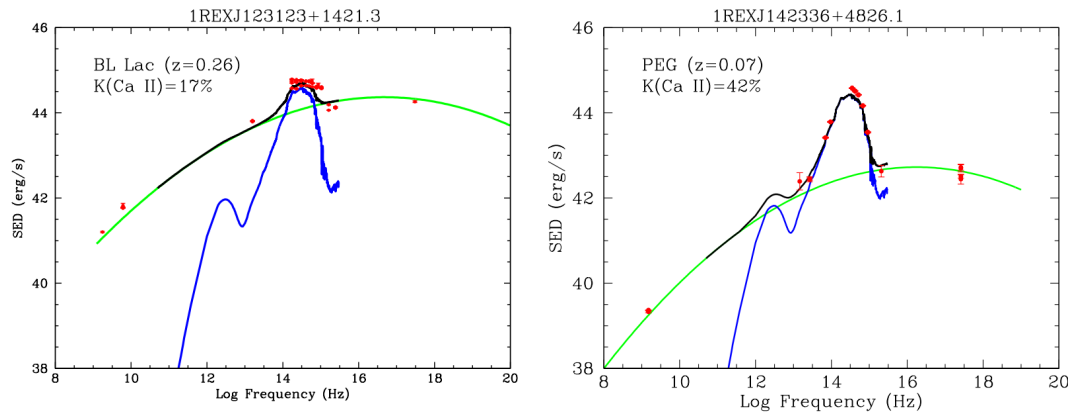


Figure 2.1: SED of BL Lac Object (left) vs. SED of PEG (right); The green line indicates the non-thermal emission of the active nucleus while the blue line indicates the thermal emission from the host galaxy. The green line is much higher in the SED of the BL Lac Object compared to the PEG [13].

Using these criteria for defining BL Lac objects and PEGs and discarding any sources with strong emission lines, the authors were left with 21 PEGs and 25 BL Lac objects to make up the final list of 46 potentially TeV-emitting REX (Te-REX) objects [13].

2.2.2 HBLs with the Highest Chance of Detection by CTA

Using the now-defined Te-REX sources, the authors predicted which of these objects would be the most likely to be detectable by CTA and current IACT observatories. A model for the predicted gamma-ray flux of the source was built using a relationship between the synchrotron peak and the ratio between the radio and x-ray flux. This model was run 1000 times for each source. Given these SEDs, the sensitivity curves of CTA and current IACT observatories were superimposed on the SEDs. The authors defined a good candidate source as a source that had at least 16% of the SEDs fall above the sensitivity curve of the observatory. Figure 2.2 shows the spectrum of an example source with each model SED shown in red [13].

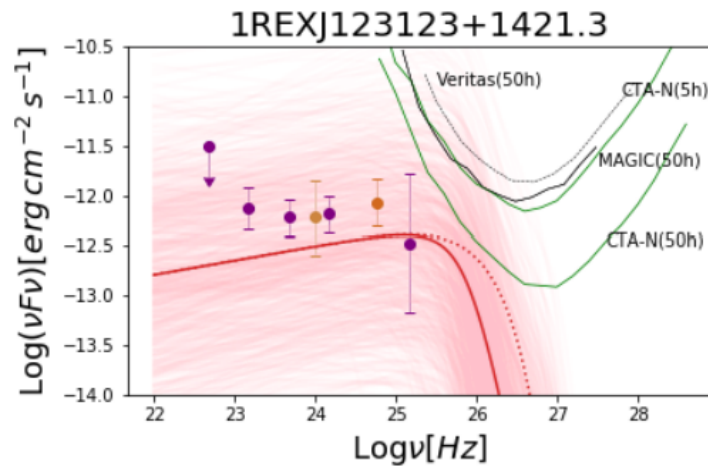


Figure 2.2: Modeled SED of 1REXJ123123+1421.3 with IACT Observatory Sensitivity Curves; Modeled SED curves indicated in red, current Fermi-LAT data indicated in purple and orange, and sensitivity curves of CTA North, Veritas, and MAGIC telescopes indicated in green. The placement of greater than 16% of the red curves above the CTA North (50 hours) and MAGIC sensitivity curves defines this source as a good candidate source for these observatories [13].

In total, 14 Te-REX sources met the requirement to be a good candidate source for CTA, and some of these 14 sources met the requirement for other current IACT observatories as well. Table 2.1 provides these sources, their classification, and the observatories for which they are determined to be a good candidate [13]. In this study, we chose these 14 sources as pre-selected candidate sources in an investigation using the HAWC Observatory.

Source Name	RA	Dec	Class	Telescopes
1REXJ121510+0732.0	12:15:10.98	+07:32:05	BL Lac	M/CTA-N
1REXJ123123+1421.3	12:31:23.89	+14:21:25	BL Lac	M/CTA-N
1REXJ125134-2958.7	12:51:34.84	-29:58:43	BL Lac	CTA-S
1REXJ133529-2950.6	13:35:29.75	-29:50:39	BL Lac	CTA-S
1REXJ134105+3959.8	13:41:05.11	+39:59:45	BL Lac	V/M/CTA-N
1REXJ141029+2820.9	14:10:29.56	+28:20:56	BL Lac	CTA-N
1REXJ141756+2543.3	14:17:56.67	+25:43:26	BL Lac	V/M/CTA-N
1REXJ142336+4826.1	14:23:36.58	+48:26:10	PEG	CTA-N
1REXJ142645+2415.3	14:26:45.52	+24:15:23	BL Lac	CTA-N
1REXJ145339+1804.2	14:53:39.96	+18:04:13	PEG	CTA-N
1REXJ151924+2053.7	15:19:24.74	+20:53:47	PEG	M/CTA-N
1REXJ154946-3045.0	15:49:46.30	-30:45:01	BL Lac	H/CTA-S
1REXJ160740+2541.2	16:07:40.60	+25:41:16	BL Lac	M/CTA-N
1REXJ183200+5202.2	18:32:00.65	+52:02:18	PEG	CTA-N

Table 2.1: Te-REX Sources Classified as “Good Candidates” for Detection by CTA; in the last column, CTA-N indicates CTA North, CTA-S indicates CTA South, M indicates the MAGIC telescopes, V indicates the Veritas telescopes, and H indicates the H.E.S.S telescopes [13].

Chapter 3

Methods

3.1 Searching for Extragalactic Very-High-Energy Gamma-Ray Sources with HAWC

At the time of this study, the HAWC Observatory has only detected three definite extragalactic sources of TeV gamma-ray emission: Mkr 421, Mkr 501 [9], and M87 [8]. Figure 3.1 shows a map of the whole sky within HAWC’s field of view, with higher \sqrt{TS} values (defined in Section 3.3) representing sources of TeV gamma-ray emission. The region created by the two curved lines of high \sqrt{TS} on the left and right are the galactic plane with galactic TeV sources, and the two small regions of high \sqrt{TS} at the center of the map are Mkr 421 and Mkr 501.

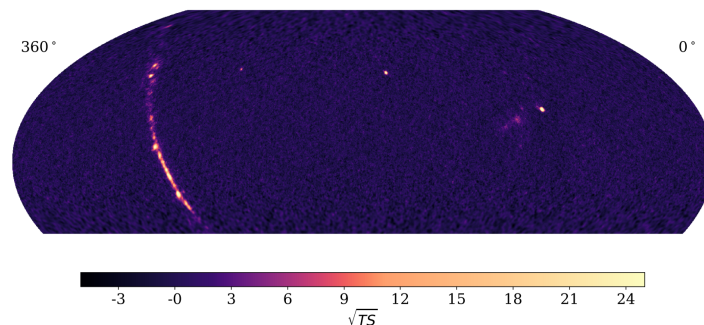


Figure 3.1: All-sky map from the HAWC Observatory. Regions of high \sqrt{TS} on the left and right are galactic sources. Two regions of high \sqrt{TS} in the center are Mkr 421 and Mkr 501 [9].

The lack of extragalactic sources of TeV emission detected by HAWC can be attributed to the attenuation of TeV gamma rays by the Extragalactic Background Light (EBL). The EBL is the sum of all the light created by stars and other processes that has been absorbed and re-emitted by dust since the beginning of the universe. Gamma rays interact with the EBL on the way to Earth, causing the gamma rays to create electrons and positrons similar to the gamma-ray showers in Earth’s atmosphere. This process is dependent on the energy of the gamma rays and the distance to the source [12]. For objects in our galaxy, the effect of the EBL is negligible for most of HAWC’s energy range of observation, but for extragalactic sources, this process is very significant. At redshifts of >0.3 , the attenuation is already in effect for the energy range of greater than a few hundred GeV [12], making it very difficult for HAWC to detect any TeV photons from these objects. Extremely high sensitivity at these energies is needed to detect these extragalactic sources in the TeV energy range.

Given the level of attenuation from extragalactic sources in the TeV energy range, any extragalactic source that is detectable by HAWC will be much fainter than galactic sources, so the method of searching for these extragalactic sources must be different than for galactic sources. Given the low levels of flux from these sources, they would be very difficult to distinguish from background fluctuations, so a blind search would likely produce thousands of candidates, of which it would be impossible to determine which are actual sources of TeV gamma-ray emission instead of background fluctuations. In this study, we instead use the “Te-REX: a sample of extragalactic TeV-emitting candidates” by Balmaverde *et al.* (see Section 2.2) to define a set of pre-selected candidate sources that can then be examined using HAWC Observatory data [13]. If gamma-ray

emission is detected at the coordinates of any of these pre-selected candidate sources, it can be attributed to these blazars and be distinguished from the background.

One caveat is that the pre-selected candidate sources were chosen in the Te-REX catalog using the sensitivity curve of CTA, not HAWC. Figure 3.2 shows the sensitivity curves of multiple observatories, including CTA and HAWC. Since CTA has a greater sensitivity than HAWC in the TeV range, these pre-selected candidate sources have a smaller chance of being detectable by HAWC than by CTA. The expected result for these pre-selected candidate sources is that they are not detectable by HAWC, but upper limits on the emission from these sources can still be calculated using the HAWC data given this lack of detection.

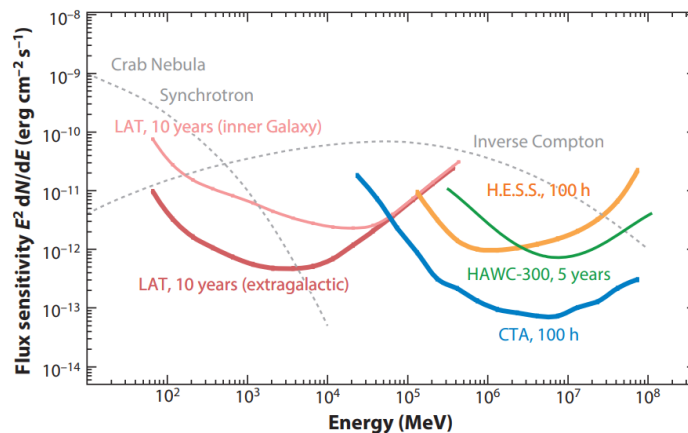


Figure 3.2: Sensitivity Curves of Various Telescopes and Observatories; note the sensitivity curves of CTA, HAWC, and Fermi-LAT (denoted LAT) [2].

3.2 Pre-Selected Candidate Sources

Returning to the list of pre-selected candidate sources from Balmaverde *et al.* (Table 2.1), we split the candidate sources into three distinct groups: sources that are outside the declination range of HAWC, sources that are within the declination range but lack lower energy data from Fermi-LAT, and sources that are both within the declination range and have lower energy data from Fermi-LAT. The sources that are outside the declination range are not candidates for further study with HAWC and will not be looked at in this study. For the sources within the declination range, different methods must be used for the groups with and without Fermi-LAT data. Information about the pre-selected candidate sources analyzed in this study is provided in Table 3.1, with sources with Fermi-LAT data noted. In total, there are eleven candidate sources considered in this study, four of which have lower energy Fermi-LAT data.

Source Name	Right Ascension	Declination	Fermi-LAT Data?
1REXJ121510+0732.0	12:15:10.98	+07:32:05	N
1REXJ123123+1421.3	12:31:23.89	+14:21:25	Y
1REXJ134105+3959.8	13:41:05.11	+39:59:45	Y
1REXJ141029+2820.9	14:10:29.56	+28:20:56	Y
1REXJ141756+2543.3	14:17:56.67	+25:43:26	Y
1REXJ142336+4826.1	14:23:36.58	+48:26:10	N
1REXJ142645+2415.3	14:26:45.52	+24:15:23	N
1REXJ145339+1804.2	14:53:39.96	+18:04:13	N
1REXJ151924+2053.7	15:19:24.74	+20:53:47	N
1REXJ160740+2541.2	16:07:40.60	+25:41:16	N
1REXJ183200+5202.2	18:32:00.65	+52:02:18	N

Table 3.1: Pre-Selected Candidate Sources from “Te-Rex: a sample of extragalactic TeV-emitting candidates” by Balmaverde *et al.* Sources with Fermi-LAT data indicated in bold and with a Y in last column [13].

3.3 Significance and Flux Upper Limit Calculations

For all sources, the calculation of the significance of a source using HAWC data is an important measure of the gamma-ray emission HAWC detects from that source. Significance is defined as the square root of the test statistic (TS) given in Equation (3.1) [8]

$$\sigma = \sqrt{TS}. \quad (3.1)$$

The test statistic is calculated through a likelihood analysis presented in Equation (3.2), where $\mathcal{L}(S + B)$ is the likelihood of the model of the source+background and $\mathcal{L}(B)$ is the likelihood of the model of the background [8]

$$TS = 2 \ln \frac{\mathcal{L}(S + B)}{\mathcal{L}(B)}. \quad (3.2)$$

A source of high-energy gamma-ray emission as detected by HAWC is defined to have a significance >5 . Significance values between 3 and 5 are considered a possible source only if a known object is located at those coordinates. Any significance less than 3 is attributed to background fluctuations. Important to this analysis is the construction of the source model, which for this analysis is a point source with a fixed simple power law index and free normalization. The simple power law index is set when calculating the significance using the Analysis and Event Reconstruction Integrated Environment (AERIE) framework designed for the analysis of HAWC data [14], and varying the index changes the assumed source model and thus the significance value for the source. AERIE was then used to calculate the differential flux of each source ($1/\text{TeV}/\text{cm}^2/\text{t}$) [14], which also depends on the assumed simple power law index. For candidate sources with low significance values, a fluxpoint cannot be calculated, and instead, the flux upper limit is calculated

as the maximum flux HAWC could be receiving and still not being able to identify the object as a source of gamma-ray emission.

3.4 Methods for Candidate Sources with Fermi-LAT Data

For the candidate sources with lower energy Fermi-LAT data, the simple power law index used for the calculations of significance values and flux upper limits was determined by fitting a simple power law to the available Fermi-LAT fluxpoints. The simple power law formula used is described in Equation (3.3) where dN/dE is the differential flux, N_0 is the normalization factor, E is the energy, E_0 is the pivot energy, set to 1 TeV in this study, and α is the simple power law index.

$$\frac{dN}{dE} = N_0 \left(\frac{E}{E_0} \right)^{-\alpha} \quad (3.3)$$

The AERIE framework was used with this simple power law index to create $5^\circ \times 5^\circ$ significance maps around the regions of each of these candidate sources [14]. Significance maps show the significance at each pixel within the region, and the significance at the center of the map (set to the location of the candidate sources) is provided. The flux upper limits of the sources at 1 TeV were also calculated using AERIE at the 95% confidence level [14]. These flux upper limits were then plotted in a log-log graph of flux vs. energy alongside the Fermi-LAT fluxpoints where they can be compared to the Fermi-LAT fluxpoints and the simple power law fit to the Fermi-LAT fluxpoints, which is extrapolated into the TeV range.

3.5 Methods for Candidate Sources without Fermi-LAT Data

For the candidate sources without lower energy Fermi-LAT data, the best simple power law indices used for the calculations of significance values and flux are not able to be determined using the same method as for the candidate sources with lower energy Fermi-LAT data. The best course of action for these sources was to examine them with three different simple power law indices: 2.0, 2.5, and 3.0. These indices were chosen based on the indices of similar sources from other studies and the indices of the candidate sources with Fermi-LAT data examined in this study. The significance maps were created and significance values at the coordinates of each candidate source, and upper limits of the flux were calculated for each of the candidate sources at each of the three indices.

Chapter 4

Results

4.1 Sources with Fermi-LAT Data

For the four pre-selected candidate sources with Fermi-LAT data, we present the Fermi-LAT fluxpoints from the 3FGL catalog, the best-fit simple power law parameters for the fit to the Fermi-LAT fluxpoints, the significance map for the $5^\circ \times 5^\circ$ region around the candidate source, the significance of the source, the calculated HAWC flux upper limit with 95% confidence level, and a spectrum showing the Fermi-LAT fluxpoints, fit to the Fermi-LAT fluxpoints, and the HAWC upper limit.

4.1.1 1REXJ123123+1421.3

1REXJ123123+1421.3 is categorized as BL Lac object by Balmaverde *et al.* and has a redshift of 0.26 [13]. The Fermi-LAT data from the 3FGL catalog over 4 years of observations on 1REXJ123123+1421.3 can be found in Table 4.1. The best-fit parameters for a simple power law fit to the Fermi-LAT data can be found in Table 4.2. The simple power law index for this source was 2.1.

Energy (MeV)	Flux ($\text{TeV}^{-1} \text{cm}^{-2} \text{s}^{-1}$)
60000	$(3.7 \pm 5.9) \times 10^{-11}$
6000	$(7.1 \pm 3.0) \times 10^{-9}$
2000	$(5.8 \pm 2.4) \times 10^{-8}$
600	$(8.1 \pm 3.9) \times 10^{-7}$

Table 4.1: Fermi-LAT Data for 1REXJ123123+1421.3 [5].

Parameter	Current Best Value
α	2.1 ± 0.1
N_0	$(1.3 \pm 1.0) \times 10^{-13} \text{TeV}^{-1} \text{cm}^{-2} \text{s}^{-1}$
E_0	1.0 TeV

Table 4.2: Parameter values for a simple power law fit to the Fermi-LAT data for 1REXJ123123+1421.3.

Using the simple power law index of 2.1, the significance map of the $5^\circ \times 5^\circ$ region surrounding 1REXJ123123+1421.3 was created using 2321 days of HAWC data (Figure 4.1). The cross at the center of the figure is located at the coordinates of 1REXJ123123+1421.3. The area of high significance at the bottom of the figure is the extragalactic source M87. Other than this small area of high significance, the significance distribution of the region is consistent with background fluctuations. The significance value and flux upper limit calculated with 2321 days of HAWC data are located in Table 4.3. The low significance of 0.24 is consistent with background fluctuations. We conclude that HAWC does not detect TeV gamma-ray emission from the coordinates of this pre-selected candidate source.

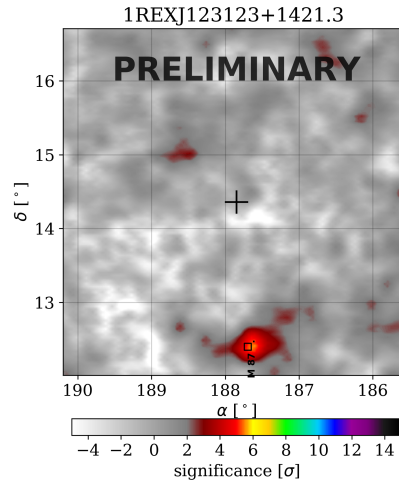


Figure 4.1: $5^\circ \times 5^\circ$ Significance map of the region around 1REXJ123123+1421.3, simple power law index of 2.1; location of 1REXJ123123+1421.3 indicated by the cross at the center of the map; area of high significance at bottom is extragalactic source M87.

α	Significance	Flux Upper Limit ($\text{TeV}^{-1} \text{cm}^{-2} \text{s}^{-1}$) at 1.0 TeV
2.1	0.24	1.85×10^{-14}

Table 4.3: HAWC significance at coordinates of 1REXJ123123+1421.3 and calculated differential flux upper limit at 1 TeV with 95% confidence level.

The low significance of this source only allows for the calculation of a HAWC flux upper limit at 1 TeV. This flux upper limit is plotted alongside the Fermi-LAT fluxpoints and the best fit to the Fermi-LAT data in Figure 4.2. This plot shows that the HAWC upper limit lies below the extrapolation of the simple power law fit into the TeV energy range. This indicates that the simple power law fit does not continue into the TeV energy range.

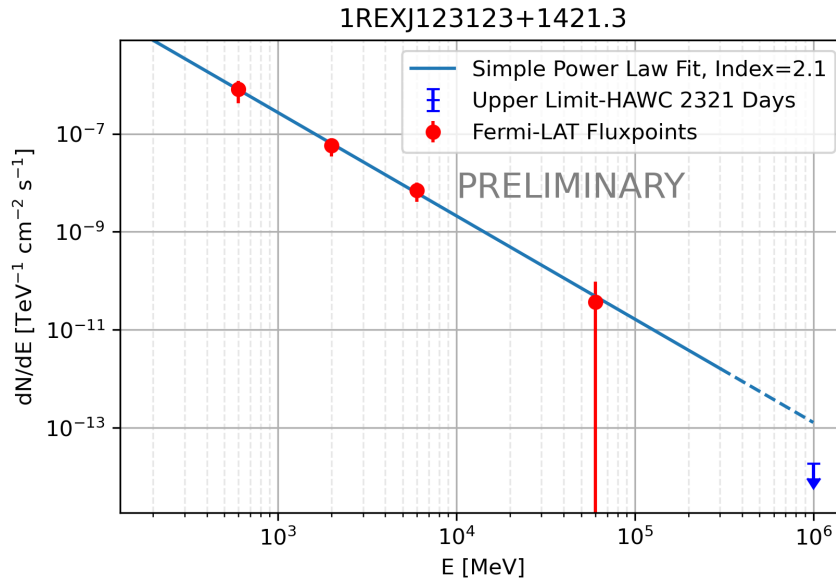


Figure 4.2: Spectrum of 1REXJ123123+1421.3.

4.1.2 1REXJ134105+3959.8

1REXJ134105+3959.8 is categorized as BL Lac object by Balmaverde *et al.* and has a redshift of 0.171 [13]. The Fermi-LAT data from the 3FGL catalog over 4 years of observations on 1REXJ134105+3959.8 can be found in Table 4.4. The best-fit parameters for a simple power law fit to the Fermi-LAT data can be found in Table 4.5. The simple power law index for this source was 2.5.

Energy (MeV)	Flux ($\text{TeV}^{-1}\text{cm}^{-2}\text{s}^{-1}$)
60000	$(1.2 \pm 1.0) \times 10^{-11}$
6000	$(3.8 \pm 1.9) \times 10^{-9}$
2000	$(2.4 \pm 1.5) \times 10^{-8}$
600	$(6.0 \pm 2.5) \times 10^{-7}$
200	$(1.5 \pm 0.5) \times 10^{-5}$

Table 4.4: Fermi-LAT Data for 1REXJ134105+3959.8 [5].

Parameter	Current Best Value
α	2.5 ± 0.1
N_0	$(4.4 \pm 1.0) \times 10^{-15} \text{ TeV}^{-1} \text{ cm}^{-2} \text{ s}^{-1}$
E_0	1.0 TeV

Table 4.5: Parameter values for a simple power law fit to the Fermi-LAT data for 1REXJ134105+3959.8.

Using the simple power law index of 2.5, the significance map of the $5^\circ \times 5^\circ$ region surrounding 1REXJ134105+3959.8 was created using 2321 days of HAWC data (Figure 4.3). The cross at the center of the figure is located at the coordinates of 1REXJ134105+3959.8. The significance distribution of the region is consistent with background fluctuations. The significance value and flux upper limit calculated with 2321 days of HAWC data are located in Table 4.6. The low significance of -1.0 is consistent with background fluctuations. The significance is negative because the observed signal from this location is less than the background signal. We conclude that HAWC does not detect TeV gamma-ray emission from the coordinates of this pre-selected candidate source.

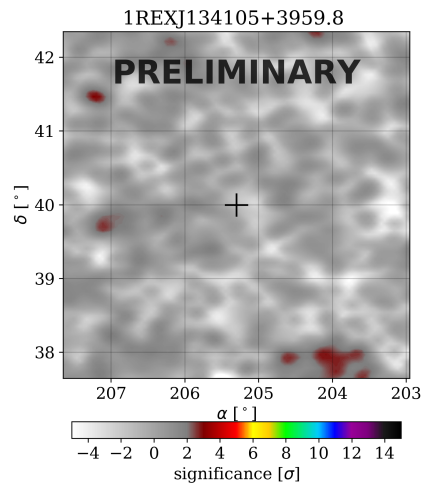


Figure 4.3: $5^\circ \times 5^\circ$ Significance map of the region around 1REXJ134105+3959.8, simple power law index of 2.5; location of 1REXJ134105+3959.8 indicated by the cross at the center of the map.

α	Significance	Flux Upper Limit ($\text{TeV}^{-1} \text{ cm}^{-2} \text{ s}^{-1}$) at 1.0 TeV
2.1	-1.0	7.83×10^{-14}

Table 4.6: HAWC significance at coordinates of 1REXJ134105+3959.8 and calculated differential flux upper limit at 1 TeV with 95% confidence level.

The low significance of this source only allows for the calculation of a HAWC flux upper limit at 1 TeV. This flux upper limit is plotted alongside the Fermi-LAT fluxpoints and the best fit to the Fermi-LAT data in Figure 4.4. This plot shows that the HAWC upper limit is slightly above the extrapolation of the simple power law fit into the TeV energy range. We cannot conclude whether the fit continues into the TeV energy range. More data will be needed to constrain this fit further.

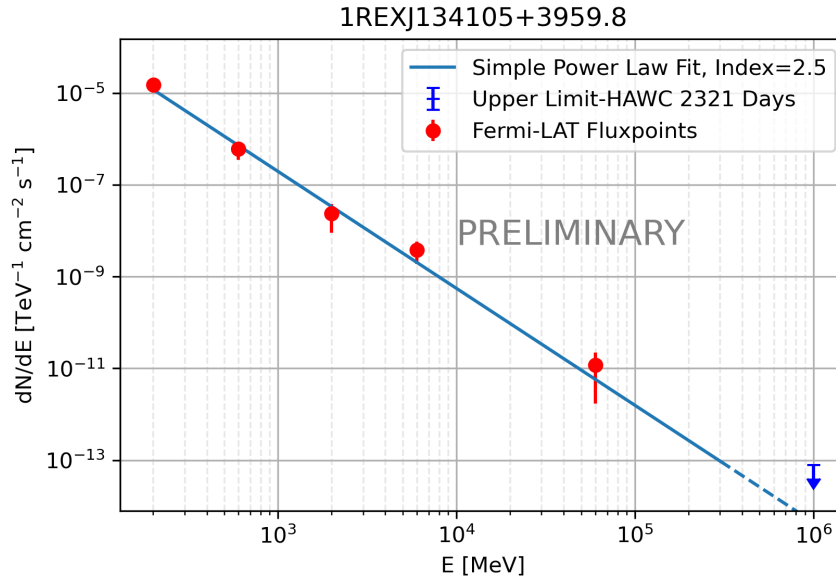


Figure 4.4: Spectrum of 1REXJ134105+3959.8.

4.1.3 1REXJ141029+2820.9

1REXJ141029+2820.9 is categorized as BL Lac object by Balmaverde *et al.* and has an unknown redshift value [13]. The Fermi-LAT data from the 3FGL catalog over 4 years of observations on 1REXJ141029+2820.9 can be found in Table 4.7. The best-fit parameters for a simple power law fit to the Fermi-LAT data can be found in Table 4.8. This simple power law was only fit to the Fermi-LAT fluxpoints and excluded the Fermi-LAT flux upper limit at 600 MeV. The simple power law index for this source was 2.2.

Energy (MeV)	Flux (TeV ⁻¹ cm ⁻² s ⁻¹)
60000	$(8.2 \pm 4.7) \times 10^{-11}$
6000	$(4.7 \pm 2.4) \times 10^{-9}$
2000	$(6.8 \pm 2.0) \times 10^{-8}$
600	$< 6.5 \times 10^{-7}$
200	$(1.1 \pm 0.6) \times 10^{-5}$

Table 4.7: Fermi-LAT Data for 1REXJ141029+2820.9 [5].

Parameter	Current Best Value
α	2.2 ± 0.1
N_0	$(9.9 \pm 1.0) \times 10^{-14} \text{ TeV}^{-1} \text{ cm}^{-2} \text{ s}^{-1}$
E_0	1.0 TeV

Table 4.8: Parameter values for a simple power law fit to the Fermi-LAT data for 1REXJ141029+2820.9.

Using the simple power law index of 2.2, the significance map of the $5^\circ \times 5^\circ$ region surrounding 1REXJ141029+2820.9 was created using 2321 days of HAWC data (Figure 4.5). The cross at the center of the figure is located at the coordinates of 1REXJ141029+2820.9. The significance distribution of the region is consistent with background fluctuations. The significance value and flux upper limit calculated with 2321 days of HAWC data are located in Table 4.9. The low significance of 0.1 is consistent with background fluctuations. We conclude that HAWC does not detect TeV gamma-ray emission from the coordinates of this pre-selected candidate source.

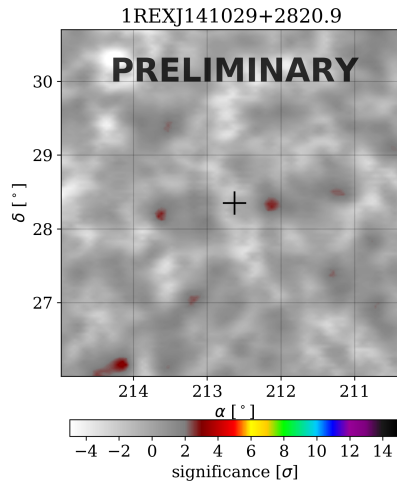


Figure 4.5: $5^\circ \times 5^\circ$ Significance map of the region around 1REXJ141029+2820.9, simple power law index of 2.2; location of 1REXJ141029+2820.9 indicated by the cross at the center of the map.

α	Significance	Flux Upper Limit ($\text{TeV}^{-1} \text{ cm}^{-2} \text{ s}^{-1}$) at 1.0 TeV
2.1	0.1	2.70×10^{-14}

Table 4.9: HAWC significance at coordinates of 1REXJ141029+2820.9 and calculated differential flux upper limit at 1 TeV with 95% confidence level.

The low significance of this source only allows for the calculation of a HAWC flux upper limit at 1 TeV. This flux upper limit is plotted alongside the Fermi-LAT fluxpoints and the best fit to the Fermi-LAT data in Figure 4.6. This plot shows that the HAWC upper limit lies below the extrapolation of the simple power law fit into the TeV energy range. This indicates that the simple power law fit does not continue into the TeV energy range.

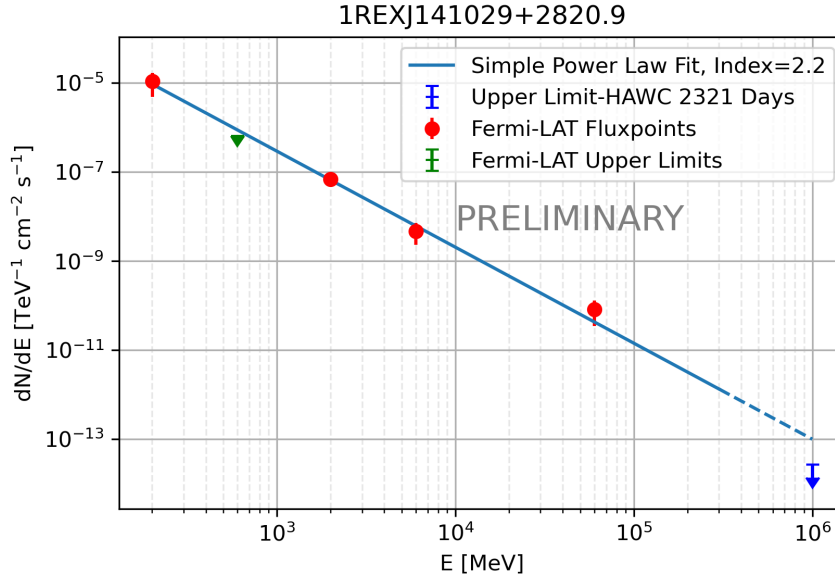


Figure 4.6: Spectrum of 1REXJ141029+2820.9.

4.1.4 1REXJ141756+2543.3

1REXJ141756+2543.3 is categorized as BL Lac object by Balmaverde *et al.* and has a redshift of 0.237 [13]. The Fermi-LAT data from the 3FGL catalog over 4 years of observations on 1REXJ141756+2543.3 can be found in Table 4.10. The best-fit parameters for a simple power law fit to the Fermi-LAT data can be found in Table 4.11. The simple power law index for this source was 2.0.

Energy (MeV)	Flux (TeV ⁻¹ cm ⁻² s ⁻¹)
60000	$(5.9 \pm 4.1) \times 10^{-11}$
6000	$(5.9 \pm 2.7) \times 10^{-9}$
2000	$(3.2 \pm 2.0) \times 10^{-8}$
600	$(6.3 \pm 3.1) \times 10^{-7}$
200	$(8.7 \pm 7.2) \times 10^{-6}$

Table 4.10: Fermi-LAT Data for 1REXJ141756+2543.3 [5].

Parameter	Current Best Value
α	2.0 ± 0.1
N_0	$(1.7 \pm 1.0) \times 10^{-13} \text{ TeV}^{-1} \text{ cm}^{-2} \text{ s}^{-1}$
E_0	1.0 TeV

Table 4.11: Parameter values for a simple power law fit to the Fermi-LAT data for 1REXJ141756+2543.3.

Using the simple power law index of 2.0, the significance map of the $5^\circ \times 5^\circ$ region surrounding 1REXJ141756+2543.3 was created using 2321 days of HAWC data (Figure 4.7). The cross at the center of the figure is located at the coordinates of 1REXJ141756+2543.3. The significance distribution of the region is consistent with background fluctuations. The significance value and flux upper limit calculated with 2321 days of HAWC data are located in Table 4.12. The low significance of -1.13 is consistent with background fluctuations. The significance is negative because the observed signal from this location is less than the background signal. We conclude that HAWC does not detect TeV gamma-ray emission from the coordinates of this pre-selected candidate source.

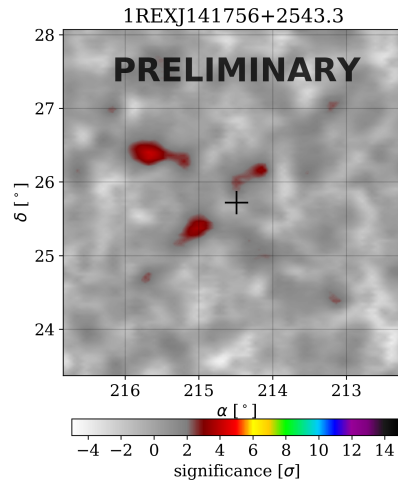


Figure 4.7: $5^\circ \times 5^\circ$ Significance map of the region around 1REXJ141756+2543.3, simple power law index of 2.0; location of 1REXJ141756+2543.3 indicated by the cross at the center of the map.

α	Significance	Flux Upper Limit ($\text{TeV}^{-1} \text{ cm}^{-2} \text{ s}^{-1}$) at 1.0 TeV
2.1	-1.13	1.54×10^{-14}

Table 4.12: HAWC significance at coordinates of 1REXJ141756+2543.3 and calculated differential flux upper limit at 1 TeV with 95% confidence level.

The low significance of this source only allows for the calculation of a HAWC flux upper limit at 1 TeV. This flux upper limit is plotted alongside the Fermi-LAT fluxpoints and the best fit to the Fermi-LAT data in Figure 4.8. This plot shows that the HAWC upper limit lies below the extrapolation of the simple power law fit into the TeV energy range. This indicates that the simple power law fit does not continue into the TeV energy range.

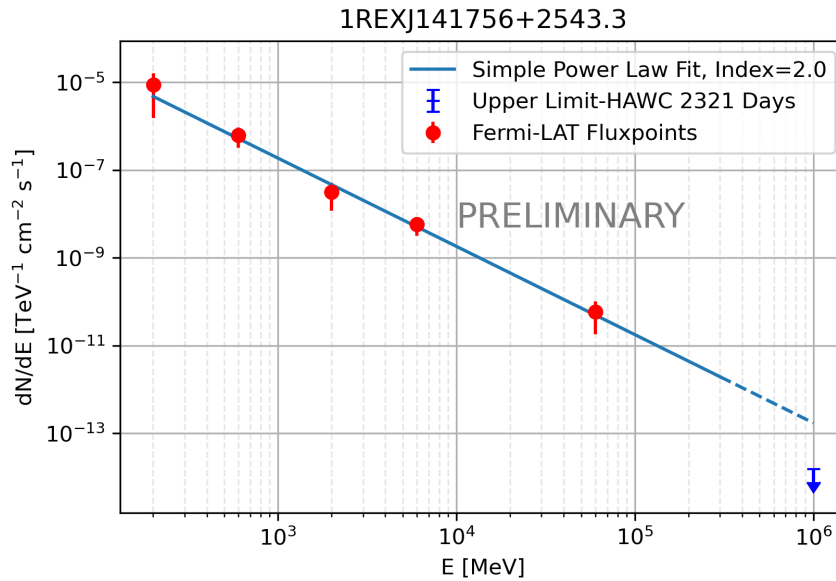


Figure 4.8: Spectrum of 1REXJ141756+2543.3.

4.2 Sources without Fermi-LAT Data

For the seven pre-selected candidate sources without Fermi-LAT data, we present the significance maps for a $5^\circ \times 5^\circ$ region around the candidate source, the significance of the source, and the calculated HAWC flux upper limit with 95% confidence level for three simple power law indices: 2.0, 2.5, and 3.0. All calculations used 2321 days of HAWC data.

4.2.1 1REXJ121510+0732.0

1REXJ121510+0732.0 is categorized as a BL Lac object by Balmaverde *et al.* and has a redshift of 0.135 [13]. Significance maps for indices 2.0, 2.5, and 3.0 are shown in Figure 4.9, created using 2321 days of HAWC data. For all three indices, the significance map is consistent with background fluctuations. The values of the significance and the flux upper limit at 1 TeV with 95% confidence level are found in Table 4.13. All three values of significance, -0.11, 0.31, and 0.33, are consistent with background fluctuations. We conclude that HAWC does not detect TeV gamma-ray emission from the coordinates of 1REXJ121510+0732.0 at simple power law indices of 2.0, 2.5, and 3.0.

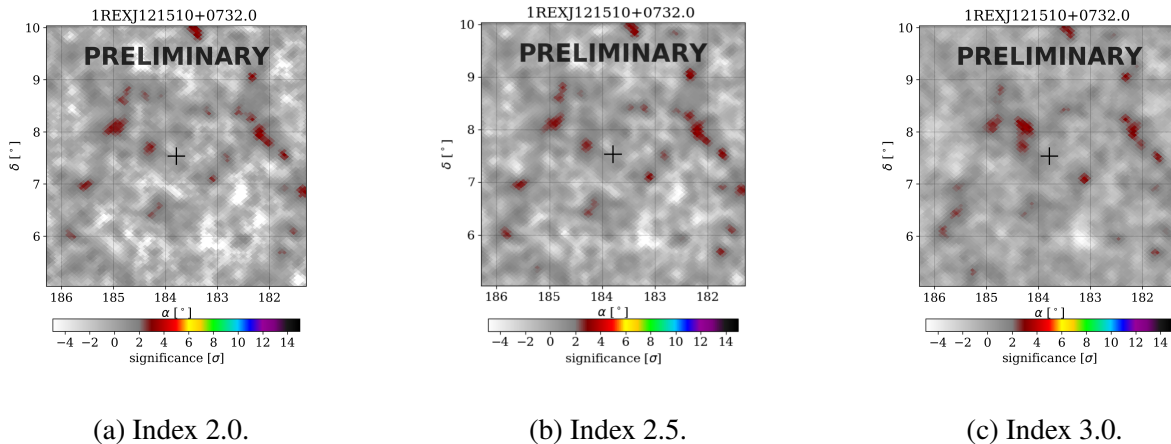


Figure 4.9: $5^\circ \times 5^\circ$ Significance maps of the region around 1REXJ121510+0732.0 with simple power law indices of 2.0, 2.5, and 3.0; location of 1REXJ121510+0732.0 indicated by the cross at the center of the map.

Simple Power Law Index (α)	Significance	Flux Upper Limit ($\text{TeV}^{-1} \text{cm}^{-2} \text{s}^{-1}$)
2.0	-0.11	1.38×10^{-14}
2.5	0.31	1.01×10^{-13}
3.0	0.33	3.92×10^{-13}

Table 4.13: HAWC significance values at coordinates of 1REXJ121510+0732.0 and calculated differential flux upper limits at 1 TeV with 95% confidence level for simple power law indices of 2.0, 2.5, and 3.0.

4.2.2 1REXJ142336+4826.1

1REXJ142336+4826.1 is categorized as a PEG object by Balmaverde *et al.* and has a redshift of 0.074 [13]. Significance maps for indices 2.0, 2.5, and 3.0 are shown in Figure 4.10, created using 2321 days of HAWC data. For all three indices, the significance map is consistent with background fluctuations. The values of the significance and the flux upper limit at 1 TeV with 95% confidence level are found in Table 4.14. All three values of significance, 0.41, 0.42, and 0.51, are consistent with background fluctuations. We conclude that HAWC does not detect TeV gamma-ray emission from the coordinates of 1REXJ142336+4826.1 at simple power law indices of 2.0, 2.5, and 3.0.

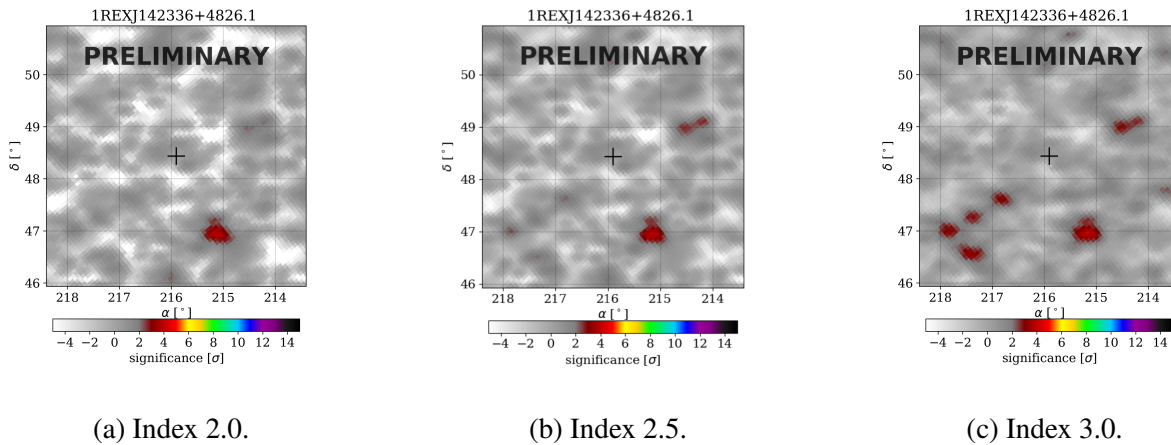


Figure 4.10: $5^\circ \times 5^\circ$ Significance maps of the region around 1REXJ142336+4826.1 with simple power law indices of 2.0, 2.5, and 3.0; location of 1REXJ142336+4826.1 indicated by the cross at the center of the map.

Simple Power Law Index (α)	Significance	Flux Upper Limit ($\text{TeV}^{-1} \text{cm}^{-2} \text{s}^{-1}$)
2.0	0.41	1.83×10^{-14}
2.5	0.42	1.32×10^{-13}
3.0	0.51	6.39×10^{-13}

Table 4.14: HAWC significance values at coordinates of 1REXJ142336+4826.1 and calculated differential flux upper limits at 1 TeV with 95% confidence level for simple power law indices of 2.0, 2.5, and 3.0.

4.2.3 1REXJ142645+2415.3

1REXJ142645+2415.3 is categorized as a BL Lac object by Balmaverde *et al.* and has an unknown redshift value [13]. Significance maps for indices 2.0, 2.5, and 3.0 are shown in Figure 4.11, created using 2321 days of HAWC data. For all three indices, the significance map is consistent with background fluctuations. The values of the significance and the flux upper limit at 1 TeV with 95% confidence level are found in Table 4.15. All three values of significance, 0.32, 0.70, and 1.51, are consistent with background fluctuations. We conclude that HAWC does not detect TeV gamma-ray emission from the coordinates of 1REXJ142645+2415.3 at simple power law indices of 2.0, 2.5, and 3.0.

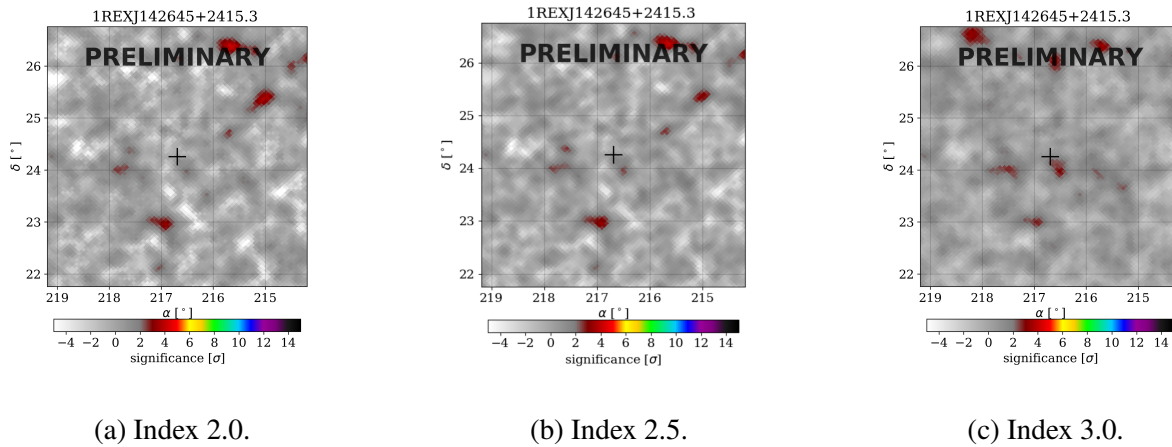


Figure 4.11: $5^\circ \times 5^\circ$ Significance maps of the region around 1REXJ142645+2415.3 with simple power law indices of 2.0, 2.5, and 3.0; location of 1REXJ142645+2415.3 indicated by the cross at the center of the map.

Simple Power Law Index (α)	Significance	Flux Upper Limit ($\text{TeV}^{-1} \text{cm}^{-2} \text{s}^{-1}$)
2.0	0.32	1.62×10^{-14}
2.5	0.70	1.10×10^{-13}
3.0	1.51	4.55×10^{-13}

Table 4.15: HAWC significance values at coordinates of 1REXJ142645+2415.3 and calculated differential flux upper limits at 1 TeV with 95% confidence level for simple power law indices of 2.0, 2.5, and 3.0.

4.2.4 1REXJ145339+1804.2

1REXJ145339+1804.2 is categorized as a PEG object by Balmaverde *et al.* and has a redshift of 0.071 [13]. Significance maps for indices 2.0, 2.5, and 3.0 are shown in Figure 4.12, created using 2321 days of HAWC data. For all three indices, the significance map is consistent with background fluctuations. The values of the significance and the flux upper limit at 1 TeV with 95% confidence level are found in Table 4.16. All three values of significance, -2.55, -2.15, and -0.58, are consistent with background fluctuations. We conclude that HAWC does not detect TeV gamma-ray emission from the coordinates of 1REXJ145339+1804.2 at simple power law indices of 2.0, 2.5, and 3.0.

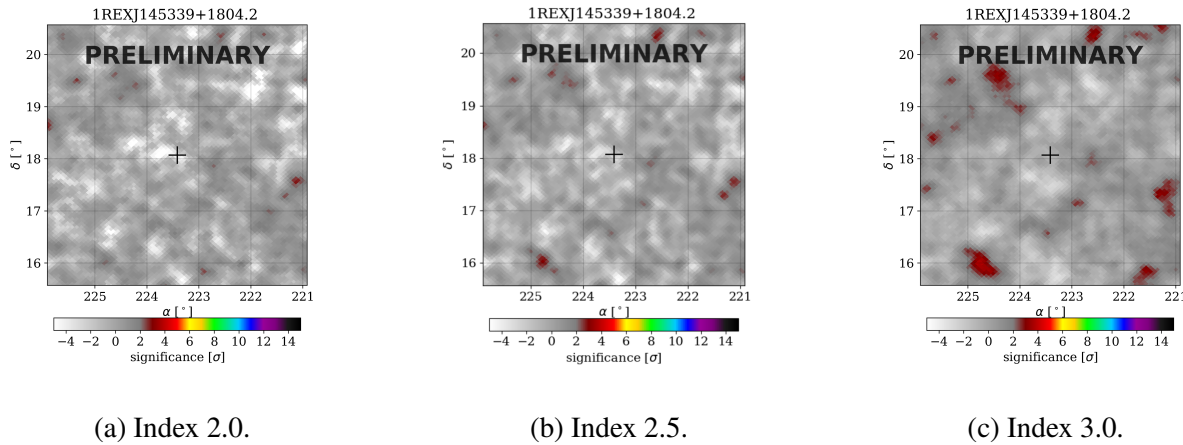


Figure 4.12: $5^\circ \times 5^\circ$ Significance maps of the region around 1REXJ145339+1804.2 with simple power law indices of 2.0, 2.5, and 3.0; location of 1REXJ145339+1804.2 indicated by the cross at the center of the map.

Simple Power Law Index (α)	Significance	Flux Upper Limit ($\text{TeV}^{-1} \text{cm}^{-2} \text{s}^{-1}$)
2.0	-2.55	4.15×10^{-15}
2.5	-2.15	3.20×10^{-14}
3.0	-0.58	1.73×10^{-13}

Table 4.16: HAWC significance values at coordinates of 1REXJ145339+1804.2 and calculated differential flux upper limits at 1 TeV with 95% confidence level for simple power law indices of 2.0, 2.5, and 3.0.

4.2.5 1REXJ151924+2053.7

1REXJ151924+2053.7 is categorized as a PEG object by Balmaverde *et al.* and has a redshift of 0.041 [13]. Significance maps for indices 2.0, 2.5, and 3.0 are shown in Figure 4.13, created using 2321 days of HAWC data. For all three indices, the significance map is consistent with background fluctuations. The values of the significance and the flux upper limit at 1 TeV with 95% confidence level are found in Table 4.17. All three values of significance, 0.25, -0.08, and 0.02, are consistent with background fluctuations. We conclude that HAWC does not detect TeV gamma-ray emission from the coordinates of 1REXJ151924+2053.7 at simple power law indices of 2.0, 2.5, and 3.0.

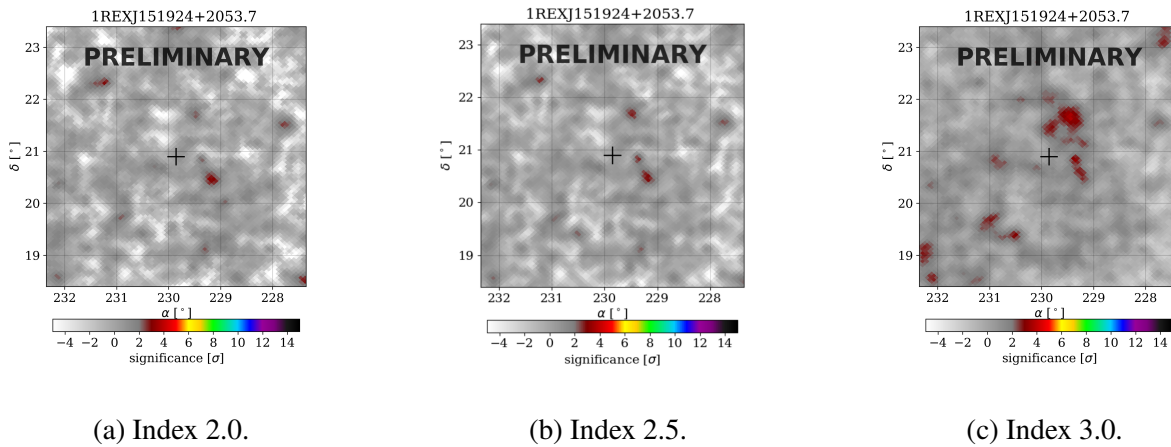


Figure 4.13: $5^\circ \times 5^\circ$ Significance maps of the region around 1REXJ151924+2053.7 with simple power law indices of 2.0, 2.5, and 3.0; location of 1REXJ151924+2053.7 indicated by the cross at the center of the map.

Simple Power Law Index (α)	Significance	Flux Upper Limit ($\text{TeV}^{-1} \text{cm}^{-2} \text{s}^{-1}$)
2.0	0.25	2.31×10^{-14}
2.5	-0.08	6.37×10^{-14}
3.0	0.02	2.83×10^{-13}

Table 4.17: HAWC significance values at coordinates of 1REXJ151924+2053.7 and calculated differential flux upper limits at 1 TeV with 95% confidence level for simple power law indices of 2.0, 2.5, and 3.0.

4.2.6 1REXJ160740+2541.2

1REXJ160740+2541.2 is categorized as a BL Lac object by Balmaverde *et al.* and has a redshift of 0.532 [13]. Significance maps for indices 2.0, 2.5, and 3.0 are shown in Figure 4.14, created using 2321 days of HAWC data. For all three indices, the significance map is consistent with background fluctuations. The values of the significance and the flux upper limit at 1 TeV with 95% confidence level are found in Table 4.18. All three values of significance, -2.10, -0.66, and 1.53, are consistent with background fluctuations. We conclude that HAWC does not detect TeV gamma-ray emission from the coordinates of 1REXJ160740+2541.2 at simple power law indices of 2.0, 2.5, and 3.0.

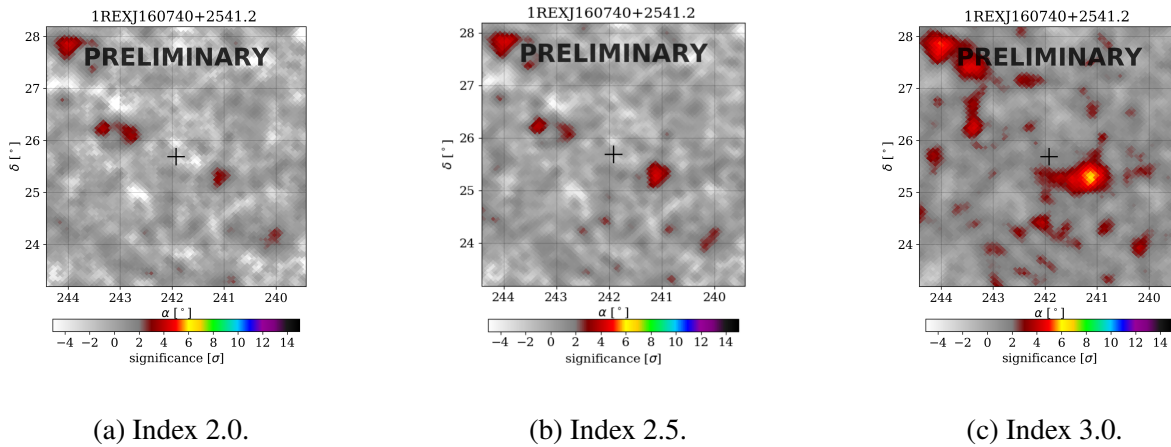


Figure 4.14: $5^\circ \times 5^\circ$ Significance maps of the region around 1REXJ160740+2541.2 with simple power law indices of 2.0, 2.5, and 3.0; location of 1REXJ160740+2541.2 indicated by the cross at the center of the map.

Simple Power Law Index (α)	Significance	Flux Upper Limit ($\text{TeV}^{-1} \text{cm}^{-2} \text{s}^{-1}$)
2.0	-2.10	6.60×10^{-15}
2.5	-0.66	6.46×10^{-14}
3.0	1.53	5.30×10^{-13}

Table 4.18: HAWC significance values at coordinates of 1REXJ160740+2541.2 and calculated differential flux upper limits at 1 TeV with 95% confidence level for simple power law indices of 2.0, 2.5, and 3.0.

4.2.7 1REXJ183200+5202.2

1REXJ183200+5202.2 is categorized as a PEG object by Balmaverde *et al.* and has a redshift of 0.046 [13]. Significance maps for indices 2.0, 2.5, and 3.0 are shown in Figure 4.15, created using 2321 days of HAWC data. For all three indices, the significance map is consistent with background fluctuations. The values of the significance and the flux upper limit at 1 TeV with 95% confidence level are found in Table 4.19. All three values of significance, 0.50, 0.47, and -0.10, are consistent with background fluctuations. We conclude that HAWC does not detect TeV gamma-ray emission from the coordinates of 1REXJ183200+5202.2 at simple power law indices of 2.0, 2.5, and 3.0.

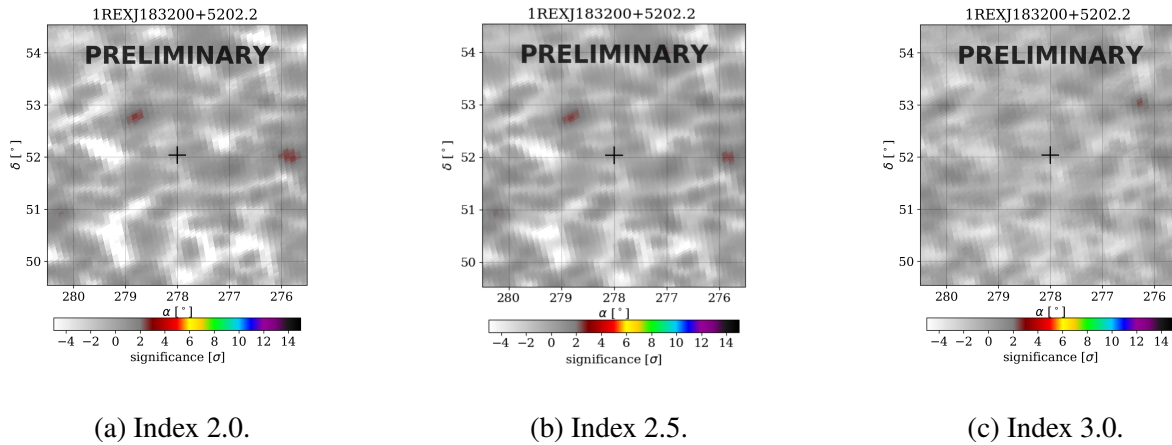


Figure 4.15: $5^\circ \times 5^\circ$ Significance maps of the region around 1REXJ183200+5202.2 with simple power law indices of 2.0, 2.5, and 3.0; location of 1REXJ183200+5202.2 indicated by the cross at the center of the map.

Simple Power Law Index (α)	Significance	Flux Upper Limit ($\text{TeV}^{-1} \text{cm}^{-2} \text{s}^{-1}$)
2.0	0.50	2.02×10^{-14}
2.5	0.47	1.39×10^{-13}
3.0	-0.10	4.80×10^{-13}

Table 4.19: HAWC significance values at coordinates of 1REXJ183200+5202.2 and calculated differential flux upper limits at 1 TeV with 95% confidence level for simple power law indices of 2.0, 2.5, and 3.0.

Chapter 5

Conclusion

5.1 Conclusion

In this study, we investigated eleven BL Lac objects with the HAWC Observatory. Four of these BL Lac objects had previous Fermi-LAT data available. Using this Fermi-LAT data we determined the best-fit simple power law equation to the spectrum of the object and used the index of this simple power law fit to investigate the source using HAWC data. We created significance maps, calculated the significance at the location of each source, and calculated the upper limit of the flux at 1 TeV for each source. For all four sources, there was no evidence of significant TeV gamma-ray emission. Given the upper limit and the Fermi-LAT data, we were able to constrain the extrapolation of the simple power law fit into the TeV energy range for three of the four sources, and for the last source, more data will be needed to determine the nature of the fit into the TeV energy ranges. For the remaining seven BL Lac objects, there was no Fermi-LAT data available, so we used three different simple power law indices to create significance maps, calculate the significance at the location of each source, and calculate the upper limit of the flux at 1 TeV for each source. For all seven objects and all three indices, there was no evidence of significant TeV gamma-ray emission. Overall, there was no significant TeV emission at the location of any of the objects we investigated using HAWC, but the upper limits we set are valuable information that can help reveal more about the spectra of the sources and the acceleration mechanisms occurring at these extreme extragalactic objects. These results were expected for such distant objects with HAWC's sensitivity at these energies, but the construction of CTA with greater sensitivity to these energies may eventually lead to the detection of these objects in the TeV energy range.

5.2 Future Work

In the future, we plan to continue to investigate extragalactic objects using HAWC in a similar manner to this study. Currently, investigations of extreme HBL objects previously observed by IACT observatories are being performed with HAWC data, and investigations of a list of BL Lac objects curated by the authors of the “Te-REX: A Sample of Extragalactic TeV-emitting Candidates” paper specifically tailored to the HAWC observatory are also being performed. We also plan to analyze the spectra of these sources outside the gamma-ray range. These objects have very strong flux in the x-ray band, so including any available x-ray data in the analysis of these sources could help determine the physical acceleration mechanisms within these objects. Fitting models of leptonic and hadronic emission mechanisms could help determine which mechanism is more dominant in the x-ray and gamma-ray energy ranges for these objects.

Bibliography

- [1] Bernard Degrange and Gérard Fontaine. Introduction to high-energy gamma-ray astronomy. *Comptes Rendus Physique*, 16(6):587–599, 2015. Gamma-ray astronomy / Astronomie des rayons gamma.
- [2] Stefan Funk. Ground- and space-based gamma-ray astronomy. *Annual Review of Nuclear and Particle Science*, 65(1):245–277, 2015.
- [3] Hugo Alberto Ayala Solares. *Search for High-Energy Gamma Rays in the Northern Fermi Bubble Region with the HAWC Observatory*. PhD thesis, Michigan Technological University, 2017.
- [4] Kathrynne Sparks Woodle. *A Likelihood Search For Very High-Energy Gamma-Ray Bursts With The High Altitude Water Cherenkov Observatory*. PhD thesis, Pennsylvania State University, 2015.
- [5] Acero F. et al. Fermi Large Area Telescope Third Source Catalog. , 218(2):23, June 2015.
- [6] Fermi gamma-ray space telescope, <https://fermi.gsfc.nasa.gov/>. *National Aeronautics and Space Administration*.
- [7] Technology, <https://www.cta-observatory.org/project/technology/>. *Cherenkov Telescope Array*.
- [8] Albert A. et al. A Survey of Active Galaxies at TeV Photon Energies with the HAWC Gamma-Ray Observatory. *The Astrophysical Journal*, 907(2):67, February 2021.
- [9] Albert A. et al. 3HWC: The Third HAWC Catalog of Very-high-energy Gamma-Ray Sources. , 905(1):76, December 2020.
- [10] About hawc, <https://www.hawc-observatory.org/>. *The High Altitude Water Cherenkov Gamma-Ray Observatory*.
- [11] Layout of the hawc observatory, <https://www.hawc-observatory.org/observatory/layout.php>. *The High Altitude Water Cherenkov Gamma-Ray Observatory*.
- [12] Elise Prandini. Highlights from tev extragalactic sources. *arxiv.org*, Jul 2007.
- [13] R. Della Ceca A. Wolter A. Belfiore L. Ballo M. Berton I. Gioia T. Maccacaro Barbara Bal-maverde, A. Caccianiga and B. Sbarufatti. Te-rex: a sample of extragalactic tev-emitting candidates. *Monthly Notices of the Royal Astronomical Society*, 492:3728–3741, March 2020.

- [14] HAWC Collaboration. The analysis and event reconstruction integrated environment (aerie) (version 2.02.00). *Gitlab Repository*, 2015.

Academic Vitae

Erica Heller

Education

Pennsylvania State University (University Park, PA) Fall 2019-Present
Bachelor of Science in Physics and Astronomy & Astrophysics
Minor in Mathematics Expected Graduation: Spring 2023

Member of Penn State University Schreyer Honors College Fall 2019-Present
Thesis Title: "Analysis of a Sample of BL Lac Objects with the HAWC Observatory"

Research Experience

Undergraduate Research Assistant 8/2021-Present
Department of Physics, Department of Astronomy & Astrophysics, Pennsylvania State University,
University Park PA

- Analyzed high-energy peaked AGNs using data from the High-Altitude Water Cherenkov (HAWC) Observatory under the supervision of Dr. Miguel Mostafá, Professor in the Department of Physics and Astronomy & Astrophysics

Summer Research Fellow 5/2022-8/2022
AAPM Summer Undergraduate Fellowship Program, Department of Medical Physics, Memorial Sloan
Kettering Cancer Center, New York NY

- Executed a research project regarding radiomics and prediction modeling of SRS-treated brain metastases under the guidance of Dr. Michalis Aristophanous, Associate Attending Physicist
- Evaluated an in-house software dealing with the change in diameter and volume of brain metastases after SRS treatment
- Shadowed clinical duties and attended departmental talks and meetings

Research Intern 1/2020-4/2021
NASA PA Space Grant Research Internship Program, Pennsylvania State University, University Park PA

- Developed and executed a research project on extragalactic sources of TeV gamma-rays with the guidance of Dr. Miguel Mostafá, Professor in the Department of Physics and Astronomy & Astrophysics

Oral Presentations

- “Te-REX Sources in HAWC”, *HAWC Collaboration Meeting*, Virtual, October 2020
- “Analysis of Te-REX Upper Limits Using HAWC Observatory Data”, *NASA PA Space Grant Internship Program Symposium*, Virtual, November 2020
- “Analysis of Te-REX Sources Using HAWC Observatory Data”, *American Physical Society Mid-Atlantic Section Meeting*, Virtual, December 2020
- “Analysis of Te-REX Sources Using HAWC Observatory Data”, *Conferences for Undergraduate Women in Physics*, Virtual, January 2021
- “Searching for multi-TeV emission from extragalactic candidates using data from the HAWC Observatory”, *American Physical Society April Meeting*, Virtual, April 2021

Poster Presentations

- “Analysis of a Sample of High-Energy Peaked BL Lac Objects with the HAWC Observatory”, *American Physical Society April Meeting*, New York, NY, April 2022

Honors

- | | |
|---|--------------|
| President’s Freshman Award | 2019 |
| <i>For academic excellence in the first semester</i> | |
| Dean’s List | 2019-2022 |
| <i>For GPA greater than 3.50 each semester</i> | |
| Homer F. Braddock Memorial Scholarship | 2019-Present |
| <i>Awarded by the Eberly College of Science, Penn State University</i> | |
| Schreyer Honors College Academic Excellence Scholarship | 2019-Present |
| <i>Awarded by the Schreyer Honors College, Penn State University</i> | |
| John and Elizabeth Holmes Teas Scholarship | 2022-Present |
| <i>Awarded by the Physics Department, Penn State University</i> | |
| Mercedes T. Richards Memorial Scholarship in Astronomy and Astrophysics | 2022 |
| <i>Awarded by the Astronomy & Astrophysics Department, Penn State University</i> | |
| Member of Sigma Pi Sigma National Physics and Astronomy Honor Society | 2022-Present |
| <i>Inducted by the Physics Department, Penn State University</i> | |
| FUTURE Ignited Program at California Institute of Technology | 2022 |
| <i>Nominated by Miguel Mostafa, Selected by the Student-Faculty Programs Office at Caltech</i> | |
| Student Representative for Braddock Scholarship Selection Committee | 2023 |
| <i>Selected by Dean Christopher Palma, Eberly College of Science, Pennsylvania State University</i> | |

Projects

Planets and Planetary Systems Final Project

Spring 2022

- Designed a mock NASA mission proposal including spacecraft design and instrumentation, planned scientific analysis, and budget.

Search for Extraterrestrial Intelligence Final Project

Fall 2021

- Compiled recent research on the current and future potential for extraterrestrial intelligence detection via transit and direct detection of exoplanet light curves

Observational Astronomy Final Project

Fall 2021

- Observed the open cluster NGC 188 with various filters using a 2' diameter optical telescope, processed the images, created H-R diagrams using stars in the field of view, and determined the age of the cluster based on the main-sequence turn-off

Quantum Mechanics II Final Project

Fall 2022

- Researched and derived the equations for a quantum mechanical electromagnetic field
- Applied these derived equations to the cases of quantum electromagnetic field fluctuations, photon absorption, and atoms in quantum electromagnetic fields

Electronics for Scientists Final Project

Fall 2022

- Designed and built a simple Theremin (electronic instrument) using both digital and analog electronic components using the human body's capacitance to change the pitch of the sound produced by the instrument

Teaching Assistance Experience

Learning Assistant

Spring 2022

Department of Physics, Pennsylvania State University, University Park PA

- Assisted the Professor in teaching students
- Answered questions about course materials from students

Employment

Grader

8/2021-Present

Department of Mathematics, Pennsylvania State University, University Park PA

- Graded homework assignments for math courses in the Department of Mathematics